American Mineralogist, Volume 89, pages 790–798, 2004

A XANES determination of the oxidation state of chromium in silicate glasses

ANDREW J. BERRY* AND HUGH ST.C. O'NEILL

Research School of Earth Sciences, Australian National University, Canberra, ACT 0200, Australia

ABSTRACT

Cr *K*-edge X-ray absorption near-edge structure (XANES) spectra were recorded for silicate glasses of various compositions in the system CaO + MgO + Al_2O_3 + SiO_2 ± TiO_2, quenched from melts equilibrated as a function of oxygen fugacity (f_{O_2}) at 1400 °C. The spectra vary systematically with f_{O_2} ($\log f_{O_2}$ ~ 0 to –16) indicating changes in the Cr oxidation state. The intensity of a shoulder on the absorption edge (attributed to the $1s \rightarrow 4s$ transition) was quantified using the corresponding peak in the XANES derivative spectrum and used to determine $Cr^{2+}/\Sigma Cr$. The resulting $Cr^{2+}/\Sigma Cr$ values are in agreement with the theoretical dependence on $\log f_{O_2}$ suggesting that the 1s → 4s feature is diagnostic of Cr^{2+} in a silicate glass and $\sigma(Cr^{2+}/\Sigma Cr) = \pm 0.015$. The $Cr^{2+}/\Sigma Cr$ ratio for a given $\log f_{O_2}$ changes with the glass composition which may reflect the ability of the melt to accommodate the Jahn-Teller distorted coordination geometry which stabilizes Cr^{2+}. $Cr^{2+}/\Sigma Cr$ varies between ~ 0.3 and 0.8 over the $\log f_{O_2}$ range bounded by the Ni/NiO and Fe/FeO f_{O_2} buffers, suggesting that Cr^{2+} may be important in natural melts even though this oxidation state has never been identified in a terrestrial material. The development of a methodology for determining $Cr^{2+}/\Sigma Cr$ from XANES spectra of quenched glasses is an essential precursor to in situ experiments on Fe-bearing silicate melts at high temperature.

INTRODUCTION

Cr is an element of potentially variable oxidation state which is found exclusively as Cr^{3+} in terrestrial materials, apart from the occurrence of Cr^{6+} in some oxidized near-surface environments (Burns and Burns 1975). However, there is strong evidence that Cr^{2+} is important in silicate melts from crystal-melt partitioning experiments which have given rise to various empirical equations to estimate the Cr^{3+}/Cr^{2+} ratio as a function of f_{O_2} (Barnes 1986; Roeder and Reynolds 1991; Hanson and Jones 1998; Poustovetov and Roeder 2000). While these experiments indicate relative changes in Cr^{3+}/Cr^{2+} they cannot yield absolute values of $Cr^{2+}/\Sigma Cr$. Circumstantial evidence for Cr^{2+} is provided by the high Cr content (> 0.1 wt% Cr_2O_3) of some natural high-temperature olivines, e.g., in komatiites, diamond inclusions, and inferred from the exsolution of chromite plus pyroxene in dunites (Li et al. 1995, and references therein). These Cr levels are consistent with a thermodynamic model in which the Cr^{2+} content of olivine in equilibrium with Cr-spinel is predicted to increase strongly with temperature (Li et al. 1995). A change from Cr^{3+} to Cr^{2+} with temperature could also explain the kink in the melt extraction trend relating the Cr and MgO contents of mantle peridotites (Liang and Elthon 1990). Cr^{2+} has been identified in Fe-free quenched silicate melts (glasses) by indirect redox titrations (wet-chemistry) and electron paramagnetic resonance spectroscopy (epr) (Schreiber and Haskin 1976). This work found that a significant proportion of ΣCr occurred as Cr^{2+} in haplobasaltic melts over the $\log f_{O_2}$ range appropriate for terrestrial magmas ($Cr^{2+}/\Sigma Cr$ up to 0.55). The absence of Cr^{2+} in Fe-bearing systems was attributed to an electron exchange reaction with Fe^{3+} ($Cr^{2+} + Fe^{3+} \rightarrow Cr^{3+} + Fe^{2+}$) arising from the large difference in the redox potentials of $Cr^{2+/3+}$ and $Fe^{2+/3+}$. The abundance of Fe relative to Cr suggested that for terrestrial $\log f_{O_2}$ values, Fe^{3+} would always occur in excess of Cr^{2+}, completely removing this oxidation state from the melt. While Cr^{2+} has never been identified in a terrestrial material, the results of the partitioning experiments clearly indicate that this oxidation state is important in Fe-bearing melts. This raises the possibility that the exchange reaction may be temperature dependent, consistent with the apparent stability of Cr^{2+} in high-temperature parageneses (Li et al. 1995), with Cr^{2+} occurring in melts but being oxidized on cooling.

There is therefore a need to directly determine $Cr^{2+}/\Sigma Cr$ in silicate melts, but as recently noted by Poustovetov and Roeder (2000) "the direct determination of (the) oxidation state of small amounts of Cr in Fe-bearing melts is not presently possible." A potential solution is X-ray absorption near-edge structure (XANES) spectroscopy, an element-specific technique which can differentiate between oxidation states and which is also suitable for the in situ study of melts. K-edge XANES spectra derive from the excitation of a 1*s* electron to higher energy bound or delocalized (continuum) excited states. Features comprising the pre-edge and edge can be attributed simplistically to transitions between bound electronic states (e.g., $1s \rightarrow 3d$, $1s \rightarrow 4s$) due to the similarity of the energy differences to those of the $(Z + 1)$ free ion levels (Shulman et al. 1976; Waychunas et al. 1983). The edge and its component transitions may vary in both energy and intensity with oxidation state. Transitions shift to higher energy with increasing charge (~ 1 eV/charge) and this trend can be used for quantifying oxidation state ratios (Wong et al. 1984; Sutton et al. 1993; Bajt et al. 1994; Berry et al. 2003a). In the case of Cr, the $1s \rightarrow 3d$, $1s \rightarrow 4s$, main edge, and edge crest all systematically vary with oxidation state (Sutton et al. 1993). The intensity of a transition is strongly dependent upon the coordina-

* E-mail: andrew.berry@anu.edu.au

tion environment since transitions such as $1s \rightarrow 3d$ and $1s \rightarrow 4s$ are symmetry forbidden but may gain intensity from orbital mixing in low-symmetry environments (Shulman et al. 1976). Different oxidation states may occupy different coordination sites resulting in transition intensities diagnostic of the redox state. Variations in coordination can also affect the energy of a feature by weighting the contribution of various component transitions to the line shape (Farges et al. 1996; Wilke et al. 2001).

Cr *K*-edge XANES spectroscopy was used to confirm the importance of Cr^{2+} in lunar olivine (Sutton et al. 1993) over 20 years after the presence of Cr^{2+} was first suggested (Haggerty et al. 1970). It has also been used to identify Cr^{6+} and determine $Cr^{6+}/\Sigma Cr$ in a variety of materials using the intensity of the $1s \rightarrow 3d$ transition (Bajt et al. 1993; Peterson et al. 1997; Szulczewski et al. 1997), to investigate the Cr^{3+} site in muscovite (Brigatti et al. 2001), and to identify unusual oxidation states such as Cr^{4+} and Cr^{5+} (Arcon et al. 1998; Levina et al. 1999).

Here we aim to develop a method for quantifying $Cr^{2+}/\Sigma Cr$ in silicate glasses and melts from XANES spectra. Spectra for a series of Fe-free silicate glasses prepared over a $\log f_{O_2}$ range for which $Cr^{2+}/\Sigma Cr$ varies from ~0 to 1 (as estimated from the results of Schreiber and Haskin 1976) should allow changes in the oxidation state to be correlated with spectral features. This work is a precursor to using XANES for the in situ determination of Cr oxidation states in Fe-bearing silicate melts at high temperatures (Berry et al. 2003b).

Experimental methods

Glasses were prepared with seven different compositions using reagent grade MgO, Al_2O_3, SiO_2, $CaCO_3$, and TiO_2 to which was added 0.5 wt% Cr_2O_3. The compositions are based on the anorthite-diopside eutectic (42% $CaAl_2Si_2O_8$ + 58% $CaMgSi_2O_6$ by weight). They include the eutectic (abbreviated as AD), four compositions derived from the eutectic by the addition of the maximum amounts of either Mg_2SiO_4 (forsterite, 15%, AD + Fo), $CaSiO_3$ (wollastonite, 60%, AD + Wo), $MgSiO_3$ (enstatite, 40%, AD + En), or SiO_2 (quartz, 40%, AD + Qz) which are soluble at 1400 °C, and two compositions containing TiO_2 (rutile, 10% and 20%, AD + Rt) (cf. O'Neill and Eggins 2002; O'Neill and Mavrogenes 2002). The average oxide compositions determined by energy-dispersive electron microprobe analysis are given in Table 1. The component reagents (mixed with polyethylene oxide and water to form a slurry) were mounted on loops of wire to enable samples to be suspended in a gas mixing vertical tube furnace at 1400 °C. The viscous melts are held on the loops by surface tension. Metals were chosen for the wires which inhibit alloying with Cr, and are stable at the $\log f_{O_2}$ of the experiment (Pt for $\log f_{O_2} \geq -8$ and Re for $\log f_{O_2} < -8$). The wire loops for a set of the six compositions were suspended from either a Pt frame or a ceramic disc with a W hook, forming a "chandelier". Ceramic is used for $\log f_{O_2} \leq -12$ where Pt corrodes due to the absorption of C from the gas environment. The melts were equilibrated using various gas mixtures to impose values of $\log f_{O_2}$ between ~–14.5 and 0; H_2/CO_2 (–14.5), CO/CO_2 (from –14 to –4), CO_2 (–3), CO_2/O_2 (from –2 to –1), and air (–0.68). The f_{O_2} of highly reduced experiments (where the error is large due to the extreme gas ratios required) was verified by simultaneously equilibrating a sample of composition CMAS7-A (from O'Neill and Eggins 2002) on an Fe loop. The f_{O_2} is related to the solubility of FeO in the melt and is given by $\log f_{O_2} = -2\log K + 2\log\gamma + 2\log X_{FeO}$ where $\log K$ is for the reaction Fe + 0.5 O_2 = FeO (Holzheid et al. 1997) and γ is the activity coefficient of FeO (O'Neill and Eggins 2002). After at least 24 hours (in most cases) the melts were quenched in water to produce glasses. Several additional samples were prepared as a function of equilibration time and ΣCr. Further details of the sample preparation techniques are given in O'Neill and Eggins (2002). Samples with $Cr^{2+}/\Sigma Cr \sim 1$ were prepared by equilibrating the Cr-free oxide mixes between layers of powdered Cr_3C_2 enclosed in a graphite capsule under flowing CO at 1 bar and 1400 °C, corresponding to $\log f_{O_2} = -16.13$. This $\log f_{O_2}$ is still several orders of magnitude more oxidizing than that required for the formation of Cr^0. Under these conditions the equilibrium Cr solubility in the melt is fortuitously close to the Cr content of the other samples (~ 0.5 wt% Cr_2O_3). These C/CO/Cr_3C_2 experiments also allow relative changes in the activity coefficient of $Cr^{2+}O$ as a function of melt composition to be determined, the results of which will be reported elsewhere. The quenched melts or glasses were mounted in epoxy and polished. Series of "calibration standards" were prepared by physically mixing powdered glasses in different proportions from two samples approximating to oxidation state end-members, i.e., $Cr^{2+}/\Sigma Cr \sim 0$ ($\log f_{O_2} = -2$) and ~ 1 ($\log f_{O_2} = -14$). These powders were pressed into pellets for analysis; in all other cases spectra were recorded from glass fragments. For the samples equilibrated at $\log f_{O_2} = -16.13$, any Cr_3C_2 associated with the glass was readily identified by optical microscopy and masked with Pb tape.

Cr *K*-edge XANES spectra were recorded in fluorescence mode at the Australian National Beamline Facility; Beamline 20B (bending magnet) at the 2.5 GeV Photon Factory (KEK, Tsukuba, Japan). The excitation energy was selected using a water-cooled Si(111) channel-cut crystal monochromator. The beam size of 2 mm (horizontal) × 1 mm (vertical) was controlled with a slit assembly 13 m from the source. The resulting energy resolution is 2.1 eV at the energy of the Cr *K*-edge, which when coupled with the Cr*K*α core-hole width of 1.08 eV (Krause and Oliver 1979), indicates a spectral energy resolution of 2.4 eV. Some spectra were also recorded using a Si(111) double-crystal sagitally focusing monochromator (Foran et al. 1998). In this case, the beam at the sample was focused to a horizontal size of 0.8 mm (FWHM at 6 keV) and the monochromator scanned in pseudo-channel-cut mode across the desired energy range. Energy was calibrated by defining the first derivative peak of Cr in stainless steel foil as 5989.2 eV. Fluorescence was measured using a Canberra GL0110S 10 element Ge array detector. The signal from each array element was passed from the detector, via a Canberra 2026XA spectroscopy amplifier (shaping time 0.25 μs), to a Canberra 2030 single channel analyzer which was set to pass the Cr*K*α signal to the counting electronics. Peak counts due to Cr*K*α photons were typically around 3500 s^{-1} per element with a total incoming count rate of less than 50000 s^{-1} per element—well within the linear response range of the detector system. The fluorescence was normalized to the incident beam flux monitored by an ionization chamber with a 30 cm path length containing 30% N_2 in He. Spectra were recorded from 5985–6025 eV using a 0.25 eV step size for a constant number of ionization chamber counts. Typical count times per point were around 5 s for a total scan time of 15–20 min. Following each scan, the signals from the ten detector elements were averaged to produce the reduced data for further analysis.

Table 1. Average glass compositions expressed as wt% oxide, excluding ~0.5 wt% Cr_2O_3

Composition	SiO_2	Al_2O_3	MgO	CaO	TiO_2
AD	50.6(6)	15.1(3)	10.3(2)	24.0(7)	–
AD + Fo	49.4(3)	13.0(2)	17.1(2)	20.5(5)	–
AD + Wo	51.5(12)	6.2(2)	4.0(2)	38.3(12)	–
AD + En	54.6(3)	9.3(2)	21.3(5)	14.8(4)	–
AD + Qz	67.8(10)	9.9(2)	6.7(2)	15.6(7)	–
AD + Rt (10%)	45.7(7)	13.7(5)	9.2(3)	21.3(10)	10.1(7)
AD + Rt (20%)	41.0(5)	12.3(1)	8.4(1)	19.6(2)	18.7(4)

Notes: The anorthite-diopside eutectic composition is abbreviated as AD; Fo = forsterite, Wo = wollastonite, En = enstatite, Qz = quartz, and Rt = rutile. There is slight compositional variability within each set of glasses due to the preparation of samples at different times from different batches of starting material.

Results

The glasses are typically transparent and homogeneous, except for the highly viscous AD + Qz composition, which is frequently translucent due to the presence of bubbles. Occasionally micro-crystals of the saturating phase were observed by optical microscopy or back-scattered electron imaging, however, these do not contain Cr or change significantly the glass composition. Crystals of $Mg(Cr,Al)_2O_4$ spinel were observed in a few samples produced at high f_{O_2}s. Glasses equilibrated under highly oxidizing conditions have lost variable amounts of Cr by volatility which may suppress the crystallization of spinel in some samples. The glasses vary in color systematically with the f_{O_2} of equilibration, ranging from blue (reduced) to green (oxidized) to yellow green (highly oxidized), with the exception of those containing TiO_2 which were brown or black when prepared under reducing

conditions (~ $\log f_{O_2} \leq -6$).

For all XANES spectra a horizontal baseline was subtracted followed by normalization to the crest of the main absorption edge. Although it is more common to normalize spectra to fluorescence above the edge, crest normalization is suitable in an empirical approach. The reduced range, and hence time, of data collection is also important for the acquisition of large data sets. Spectra for Cr in stainless steel foil (Cr^0), K_2CrO_4 (Cr^{6+}), and AD glasses prepared at $\log f_{O_2} = -14$ (Cr^{2+}) and –2 (Cr^{3+}) are shown in Figure 1. The AD glasses contain Cr predominantly in the oxidation state indicated (see below), as expected from both their color and the results of Schreiber and Haskin (1976). The spectra show the expected shift of the main absorption edge to higher energies with increasing oxidation state. The Cr^{6+} spectrum is characterized by a very intense $1s \rightarrow 3d$ pre-edge transition. The main difference between the nominal Cr^{2+} and Cr^{3+} spectra, apart from the edge shift, is the appearance of an intense shoulder on the Cr^{2+} absorption edge assigned as the $1s \rightarrow 4s$ transition (Sutton et al. 1993). This transition is symmetry forbidden but may gain intensity from orbital mixing in low-symmetry environments. Due to the coordination freedom available in a melt, Cr can adopt the coordination geometry for each oxidation state that produces the greatest electronic stabilization. The high-symmetry octahedral geometry favored by Cr^{3+} (d^3) results in the $1s \rightarrow 4s$ feature being weak or absent, whereas the transition becomes allowed for Cr^{2+} (d^4) due to a Jahn-Teller distortion of the coordination environment. The absorption edge shoulder may therefore be diagnostic of Cr^{2+} in a silicate melt, which suggests that its intensity may be used to quantify $Cr^{2+}/\Sigma Cr$.

The Cr^{2+} and Cr^{3+} spectra in Figure 1 are reproduced in Figure 2a together with spectra for a series of physical mixtures of these two "end-members" which represent 10% increments in nominal $Cr^{2+}/\Sigma Cr$. As expected, there is a systematic trend in the edge energy and the intensity of the $1s \rightarrow 4s$ shoulder. The $1s \rightarrow 4s$ intensity is most easily quantified from the derivative spectrum in which the shoulder appears as a well-resolved peak. The integrated area of this peak from 5991.3–5996.3 eV for the spectra in Figure 2b, is linearly correlated with the nominal $Cr^{2+}/\Sigma Cr$ value, as shown in Figure 3. The choice of integral range is somewhat arbitrary, has little effect on the correlation (only changing the slope and offset), and is not important in an empirical approach. The correlation in Figure 3 thus provides an empirical calibration curve for determining $Cr^{2+}/\Sigma Cr$ in a glass of this composition. The derivative spectra shown in Figure 2b (and Fig. 4b) have

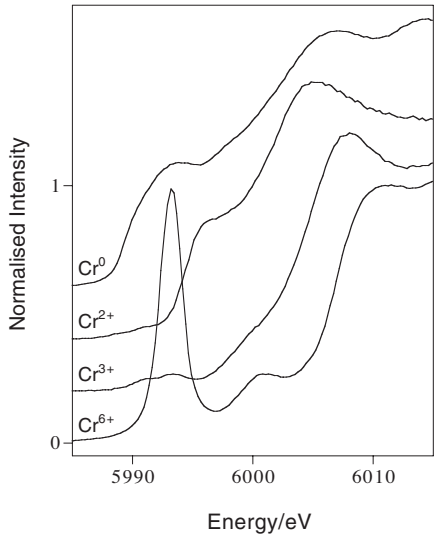

FIGURE 1. Cr *K*-edge XANES spectra for Cr in stainless steel foil (Cr^0), Cr in anorthite-diopside eutectic (AD) glasses quenched from melts equilibrated at 1400 °C and $\log f_{O_2} = -14$ (Cr^{2+}) and –2 (Cr^{3+}), and K_2CrO_4 (Cr^{6+}).

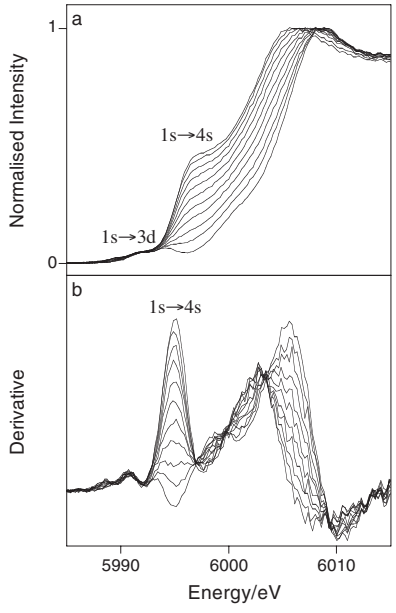

FIGURE 2. (**a**) Cr *K*-edge XANES spectra and (**b**) the corresponding derivative spectra, for physical mixtures of nominal Cr^{2+} ($\log f_{O_2} = -14$) and Cr^{3+} ($\log f_{O_2} = -2$) end-member AD glasses, representing ~ 10% increments in $Cr^{2+}/\Sigma Cr$. The spectra vary systematically with $Cr^{2+}/\Sigma Cr$. Features comprising the absorption edge are assigned to the electronic transitions indicated.

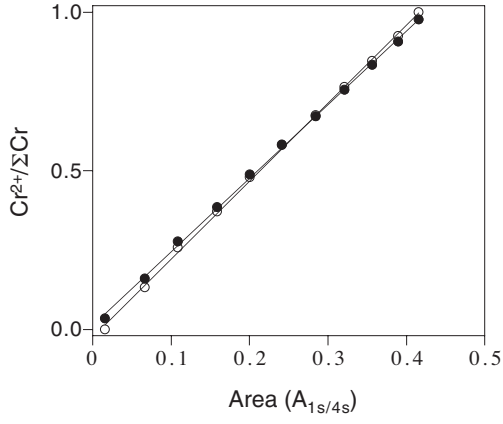

FIGURE 3. Correlation between $Cr^{2+}/\Sigma Cr$, for mixtures of nominal Cr^{2+} and Cr^{3+} end-member AD glasses, and the area of the $1s \rightarrow 4s$ peak ($A_{1s/4s}$) in the XANES derivative spectrum (Fig. 2). The open symbols correspond to the $Cr^{2+}/\Sigma Cr$ content assuming $Cr^{2+}/\Sigma Cr = 1$ and 0 in the end-members and the filled symbols represent $Cr^{2+}/\Sigma Cr$ determined using the corrected $Cr^{2+}/\Sigma Cr$ values of the end-members found by fitting the $\log f_{O_2}$ series to Equation 5 (Fig. 5).

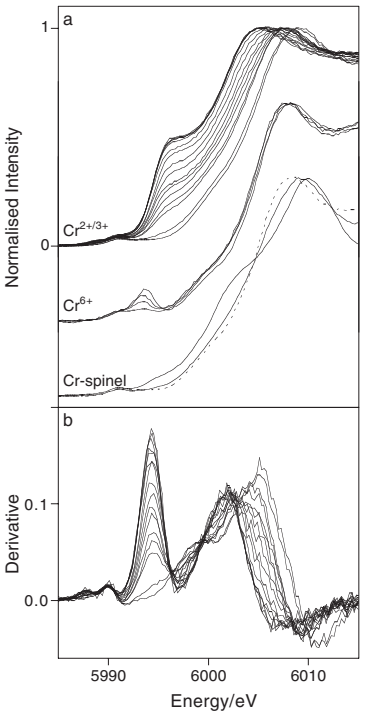

FIGURE 4. (**a**) Cr *K*-edge XANES spectra for AD + En glasses prepared at 16 values of $\log f_{O_2}$ ranging from –16.13 to –3 ($Cr^{2+/3+}$), and (**b**) the corresponding derivative spectra. Spectra are also shown for AD + Wo glasses equilibrated at $\log f_{O_2} = -2.0, -1.5, -1.0$, and -0.68 (Cr^{6+}), and two samples exhibiting slight (AD + En, $\log f_{O_2} = -4$) and severe (AD + Qz, $\log f_{O_2} = -7$) contamination by Cr-spinel (Cr-spinel). The dashed line is a Cr-spinel-free Cr^{3+} spectrum for comparison.

been smoothed using a five point moving average, however, the areas were determined from the unsmoothed data.

XANES spectra for the AD + En composition equilibrated at different values of f_{O_2} are shown in Figure 4. Since f_{O_2} is the only variable in the sample preparation, and for this f_{O_2} range Cr is the only redox variable element, changes in the spectra must reflect changes in the Cr oxidation state. The intensity of the $1s \rightarrow 4s$ transition decreases systematically with increasing f_{O_2} as would be expected for oxidation of Cr^{2+} to Cr^{3+}. For highly oxidized samples ($\log f_{O_2} \geq -2$) a pre-edge feature appears which increases in intensity with increasing f_{O_2}. This transition is diagnostic of Cr^{6+} (Fig. 1) and those samples containing this oxidation state are readily identified (Fig. 4, Cr^{6+}). Some glasses contain crystals of Cr-spinel, resulting in a characteristic shift of the edge crest to higher energy and a distinctive XANES spectrum (Fig. 4, Cr-spinel). The XANES spectra thus not only provide a quantifiable feature that is diagnostic of Cr^{2+}, but also identify samples where competing processes may affect the f_{O_2} dependence of the $Cr^{2+}/\Sigma Cr$ ratio.

The reaction describing the oxidation of a metal, as an oxide component in a melt is,

$$M^{x+}O_{x/2} + n/4O_2 = M^{(x+n)+}O_{(x+n)/2} \text{ or } Cr^{2+}O + 1/4O_2 = Cr^{3+}O_{3/2} \quad (1)$$

where n is the number of electrons involved in the oxidation. The equilibrium constant for this reaction is:

$$K = \frac{X_{M^{(x+n)+}O_{(x+n)/2}} \gamma_{M^{(x+n)+}O_{(x+n)/2}}}{X_{M^{x+}O_{x/2}} \gamma_{M^{x+}O_{x/2}} (f_{O_2})^{n/4}} \quad \text{or}$$

$$K = \frac{X_{Cr^{3+}O_{1.5}} \gamma_{Cr^{3+}O_{1.5}}}{X_{Cr^{2+}O} \gamma_{Cr^{2+}O} (f_{O_2})^{1/4}} \quad (2)$$

where X is the mole fraction and γ the activity coefficient. This leads to:

$$\log \frac{X_{M^{(x+n)+}O_{(x+n)/2}}}{X_{M^{x+}O_{x/2}}} = n/4 \log f_{O_2} + \log K - \log \left(\frac{\gamma_{M^{(x+n)+}O_{(x+n)/2}}}{\gamma_{M^{n+}O_{x/2}}} \right)$$

or (3)

$$\log \frac{X_{Cr^{3+}O_{1.5}}}{X_{Cr^{2+}O}} = \log \frac{[Cr^{3+}]}{[Cr^{2+}]} = 1/4 \log f_{O_2} + \log K - \log \left(\frac{\gamma_{Cr^{3+}O_{1.5}}}{\gamma_{Cr^{2+}O}} \right).$$

For low Cr concentrations, $\gamma_{Cr3+O1.5}$ and γ_{Cr2+O} may be assumed to be constant for a given melt composition (Henry's Law). Accordingly we define:

$$\log K' = \log K - \log \left(\frac{\gamma_{Cr^{3+}O_{1.5}}}{\gamma_{Cr^{2+}O}} \right) \quad (4)$$

where K' is the K for reaction 1 in a particular melt composition. Assuming $[Cr^{2+}] + [Cr^{3+}] = [\Sigma Cr]$, rearrangement of this equation gives a sigmoidal function describing the f_{O_2} dependence of the oxidation state:

$$\frac{M^{x+}}{\Sigma M} = \frac{1}{1 + 10^{\left(n/4 \log f_{O_2} + \log K'\right)}} \text{ or } \frac{Cr^{2+}}{\Sigma Cr} = \frac{1}{1 + 10^{\left(1/4 \log f_{O_2} + \log K'\right)}} \quad (5)$$

The physical mixtures of "end-members" for the AD (Fig. 3) and AD + En compositions provide calibration curves describing the relationship between the derivative peak area ($A_{1s/4s}$) and $Cr^{2+}/\Sigma Cr$. These curves allow $A_{1s/4s}$ to be converted to $Cr^{2+}/\Sigma Cr$ for each $\log f_{O_2}$ value of the f_{O_2} series, and the results were fit to Equation 5 by multiple non-linear least-squares regression with $n/4$ and $\log K'$ as variables. The resulting best fit indicates that the Cr^{2+} ($\log f_{O_2} = -14$) and Cr^{3+} ($\log f_{O_2} = -2$) "end-members" actually contain several percent of ΣCr as Cr^{3+} and Cr^{2+} respectively. The $Cr^{2+}/\Sigma Cr$ values for each physical mixture were recalculated, producing a modified calibration curve, and the fitting process repeated. The new fit again suggests refinement of the $Cr^{2+}/\Sigma Cr$ content of the end-members and the procedure was iterated until the solution converged. An exponent of 0.257 ± 0.010 was obtained for AD and 0.249 ± 0.006 for AD + En, in excellent agreement with the theoretical value of 0.25. The refined $Cr^{2+}/\Sigma Cr$ values of the calibration mixtures are given in Table 2 and the final calibration curve for AD is shown in Figure 3. The relationship between $A_{1s/4s}$ and $Cr^{2+}/\Sigma Cr$ is linear and the χ^2 of the fit to the calibration data is consistent with $\sigma(A_{1s/4s}) = 0.005$.

Since $A_{1s/4s}$ is a linear function of $Cr^{2+}/\Sigma Cr$,

$$Cr^{2+}/\Sigma Cr = a_0 + a_1 A_{1s/4s} \quad (6)$$

where a_0 and a_1 are constants for each melt composition (the "calibration constants"). Combining Equations 5 and 6 gives,

$$A_{1s/4s} = \frac{1}{a_1} \left(\frac{1}{1 + 10^{\left(n/4 \log f_{O_2} + \log K'\right)}} - a_0 \right). \quad (7)$$

This equation indicates that a_0, a_1, $n/4$, and $\log K'$ may be determined simultaneously for a suite of samples prepared over a range of f_{O_2}s. The experimental values of $A_{1s/4s}$ for all compositions and $\log f_{O_2}$ values are given in Table 3. $A_{1s/4s}$ plotted against $\log f_{O_2}$ defines the expected sigmoidal function. The value of $A_{1s/4s}$ at $\log f_{O_2} = -11$ was determined from three different spectra recorded at different times using both monochromators. These replicate points suggest that the error associated with determining $A_{1s/4s}$ is small. Uncertainties of ± 0.005 in $A_{1s/4s}$ and ± 0.03 in $\log f_{O_2}$ for $\log f_{O_2} > -12$ and ± 0.1 for $\log f_{O_2} \leq -12$ were assumed (all uncertainties are one standard deviation). Not all points were used in fitting the data. Those derived from spectra which indicate the presence of significant Cr-spinel or Cr^{6+} were excluded. Also excluded were the points for AD at $\log f_{O_2} = -7$ and AD + Qz at $\log f_{O_2} = -12$, which are anomalous for no apparent reason, and all points at $\log f_{O_2} = -14.5$ for which the $A_{1s/4s}$ values are lower than expected (probably due to the volatile loss of SiO_2 at this extremely reduced condition).

TABLE 2. The 1s → 4s peak areas ($A_{1s/4s}$) in Cr K-edge XANES derivative spectra of various mixtures of two oxidation state "end-member" powdered glasses; $(Cr^{2+}/\Sigma Cr)_{-14} \sim 1$ ($\log f_{O_2} = -14$) and $(Cr^{2+}/\Sigma Cr)_{-2} \sim 0$ ($\log f_{O_2} = -2$)

AD			AD + En		
Area	M_{-14}	$Cr^{2+}/\Sigma Cr$	Area	M_{-14}	$Cr^{2+}/\Sigma Cr$
0.015	0.0	0.035(6)	0.016	0.0	0.047(5)
0.067	0.1	0.161(6)	0.065	0.1	0.176(10)
0.109	0.2	0.278(7)	0.112	0.2	0.294(16)
0.159	0.3	0.386(7)	0.154	0.3	0.401(18)
0.201	0.4	0.488(7)	0.203	0.4	0.499(19)
0.241	0.5	0.583(7)	0.242	0.5	0.589(18)
0.285	0.6	0.672(6)	0.292	0.6	0.672(16)
0.322	0.7	0.755(6)	0.336	0.7	0.750(13)
0.357	0.8	0.834(5)	0.365	0.8	0.821(10)
0.390	0.9	0.908(4)	0.397	0.9	0.888(5)
0.416	1.0	0.978(4)	0.424	1.0	0.950(2)

Note: The $Cr^{2+}/\Sigma Cr$ of each mixture is given by:

$$\frac{Cr^{2+}}{\Sigma Cr} = \frac{\left(Cr^{2+}/\Sigma Cr\right)_{-14}[\Sigma Cr]_{-14}M_{-14} + \left(Cr^{2+}/\Sigma Cr\right)_{-2}[\Sigma Cr]_{-2}M_{-2}}{[\Sigma Cr]_{-14}M_{-14} + [\Sigma Cr]_{-2}M_{-2}}$$

where [ΣCr] is the Cr content and M the mass fraction ($M_{-2} = 1 - M_{-14}$). For AD, $[\Sigma Cr]_{-14} = 3561 \pm 49$ ppm and $[\Sigma Cr]_{-2} = 2572 \pm 56$ ppm; for AD + En, $[\Sigma Cr]_{-14} = 3487 \pm 10$ ppm and $[\Sigma Cr]_{-2} = 2321 \pm 195$ ppm. $(Cr^{2+}/\Sigma Cr)_{-14,-2}$ were estimated from the fit of the $\log f_{O_2}$ series data shown in Figure 5a,d to Equation 5. Uncertainties (1 σ) include the errors in ΣCr and $(Cr^{2+}/\Sigma Cr)_{-14,-2}$ (from the error in $\log K'$).

The f_{O_2} series data (Table 3) were fit directly to Equation 7. In the first instance the exponent $n/4$ was allowed to vary and the calculated values, given in Table 4, are in good agreement with the theoretical value of 0.25 for four out of the five TiO_2-free compositions. The exception is AD + Fo for which all data at $\log f_{O_2} \geq -6.5$ are contaminated with either spinel or Cr^{6+}. The fit to the resulting reduced data set was constrained by fixing a_0 at 0.029, the weighted average value determined for the other compositions, giving an exponent of 0.284(12). This exponent is anomalously large and strongly correlated with the value of $\log K'$, which is also anomalous, suggesting that the deviation from the expected value may result from the lack of data at oxidized conditions. There are insufficient data to determine the exponents for the TiO_2-containing compositions. The values of $n/4$, a_0, and a_1 for AD and AD + En are also in excellent agreement with those obtained from the calibration curves.

The exponent was then fixed at 0.25 and the fit to Equation 7 repeated for all compositions. These results are also given in Table 4. The fits to the data are excellent and are shown in Figure 5, where $A_{1s/4s}$ has been converted to $Cr^{2+}/\Sigma Cr$ using Equation 6 and the values of a_0 and a_1 in Table 4. Points excluded from the fit are

TABLE 3. The 1*s* → 4*s* derivative peak areas ($A_{1s/4s}$) and corresponding $Cr^{2+}/\Sigma Cr$ values determined from Equation 6 using the parameters in Table 4 for the fit to Equation 7

$\log f_{O_2}$	AD		AD + Fo		AD + Wo		AD + En		AD + Qz		AD + Rt§§	
	$A_{1s/4s}$	$Cr^{2+}/\Sigma Cr$	$A_{1s/4s}$	$Cr^{2+}/\Sigma Cr$	$A_{1s/4s}$	$Cr^{2+}/\Sigma Cr$	$A_{1s/4s}$	$Cr^{2+}/\Sigma Cr$	$A_{1s/4s}$	$Cr^{2+}/\Sigma Cr$	$A_{1s/4s}$	$Cr^{2+}/\Sigma Cr$
–0.68*	0.005	0.050**	0.009	0.050**	0.008	0.032**	0.008	0.037**	0.007	0.062**	0.014	–0.033**,||||
–1.0†	0.029	0.105**	0.024	0.082**	0.016	0.055**	0.026	0.077**	0.031	0.114**	0.020	–0.033**
–1.5†	0.034	0.116**	0.033	0.102**	0.024	0.073**	0.034	0.095**	0.028	0.108**	0.029	–0.006**
–2.0†	0.024	0.094**	0.020	0.075**	0.020	0.063**	0.021	0.065**	0.022	0.096**	0.023	–0.024**
"											0.028	–0.010**
–3.0‡	0.017	0.078	0.026	0.087††	0.018	0.057	0.024	0.071	0.029	0.110	0.031	–0.003
–4.0	0.039	0.128††	0.034	0.105††	0.026	0.080	0.050	0.128	0.065	0.187	0.049	0.047
–5.0	0.060	0.175††			0.044	0.124	0.063	0.157††			0.058	0.086||||
–6.0	0.118	0.307	0.089	0.229††	0.085	0.229	0.138	0.322	0.173	0.421	0.080	0.130
–6.5	0.140	0.357	0.116	0.290††	0.099	0.264	0.163	0.375	0.199	0.476	0.098	0.179
–7.0	0.244	0.591	0.151	0.368	0.123	0.325	0.190	0.434	0.081	0.222††	0.114	0.233||||
–7.5	0.207	0.507	0.196	0.470	0.156	0.407	0.232	0.527	0.263	0.614	0.127	0.258
–8.0	0.231	0.563	0.233	0.553	0.174	0.453	0.249	0.563	0.294	0.680		
–8.5	0.271	0.654	0.264	0.622	0.209	0.542	0.293	0.659	0.333	0.766	0.174	0.384
–9.0	0.296	0.709	0.297	0.697	0.234	0.606	0.328	0.736	0.348	0.798	0.210	0.488||||
–10.0			0.347	0.809	0.293	0.755	0.374	0.836	0.390	0.889	0.235	0.551
–11.0	0.382	0.903	0.385	0.893	0.325	0.836	0.391	0.873	0.411	0.934	0.315	0.767||||
"	0.386	0.913	0.381	0.885	0.329	0.848	0.394	0.879	0.412	0.936	0.304	0.737||||
"	0.379	0.897	0.387	0.898	0.329	0.847	0.392	0.875	0.412	0.936		
–12.0	0.384	0.908	0.388	0.900	0.333	0.856	0.408	0.910	0.388	0.883	0.331	0.809||||
–12.7#	0.396	0.936‡‡	0.396	0.919‡‡	0.357	0.916	0.440	0.979	0.415	0.942	0.369	0.908||||
"							0.417	0.930			0.368	0.906||||
–13.75#	0.417	0.983	0.420	0.973	0.382	0.980	0.445	0.991	0.437	0.989	0.375	0.930
–14.5§	0.394	0.930			0.357	0.918			0.411	0.933	0.382	0.951
–16.13||	0.423	0.997	0.431	0.998	0.385	0.989	0.446	0.992	0.441	0.999		

Notes: The uncertainty (1 σ) in $A_{1s/4s}$ is ± 0.005. $\log f_{O_2}$ imposed by CO/CO_2 except for *air, †CO_2/O_2, ‡CO_2, §H_2/CO_2, and ||Cr_2C_3/CO.
$\log f_{O_2}$ determined from Fe/CMAS.
** samples containing Cr^{6+}.
†† samples containing Cr–spinel.
‡‡ intermediate composition between AD and AD + 15% Mg_2SiO_4 suggesting melts were in contact during equilibration.
§§ AD + Rt (20%) except for |||| which correspond to AD + Rt (10%).

TABLE 4. Parameters obtained from fitting the data in Table 3 to Equation 7

Composition	*n*/4	log*K'*	a_0	a_1	*p*	χ^2
AD	0.257(12)	1.871(17)	0.039(10)	2.265(24)	14	1.44
AD + Fo	0.284(12)	1.921(12)	0.029*	2.247(14)	11	2.91
AD + Wo	0.250(12)	2.056(18)	0.013(10)	2.534(26)	16	1.55
AD + En	0.244(11)	1.844(16)	0.020(10)	2.181(23)	15	1.68
AD + Qz	0.254(13)	1.650(19)	0.048(12)	2.154(27)	13	1.44
AD + Rt (10%)	–	2.274(43)	–0.069(19)	2.650(49)	6	2.31
AD + Rt (20%)	–	2.371(26)	–0.086(10)	2.711(37)	8	2.28

Note: n/4 is the calculated exponent while log*K'*, a_0, and a_1, were all determined for a fixed theoretical exponent of 1/4. *p* is the number of data points used in the fit. There are insufficient data to determine *n*/4 for the TiO_2-containing compositions.
* Fixed at 0.029.

indicated. For AD + Fo, a_0 was again set to 0.029, with the χ^2 of the resulting fit indicating that the data can be satisfactorily described using the theoretical exponent. The two TiO_2 containing compositions are fit well by Equation 7, giving similar values of a_0, a_1, and log*K*', although a non-ideal value of the exponent cannot be excluded. The fit to AD + Rt (20%) is shown in Figure 5f. The replicate points at $\log f_{O_2} = -11$ are all plotted in Figures 5a–f, illustrating the precision with which $Cr^{2+}/\Sigma Cr$ can be determined. The overall uncertainties are smaller than the size of the symbols. The $Cr^{2+}/\Sigma Cr$ values for the samples containing Cr-spinel are all lower than that calculated (Figs. 5b and 5d). This is consistent with the change in Cr^{2+}/Cr^{3+} expected

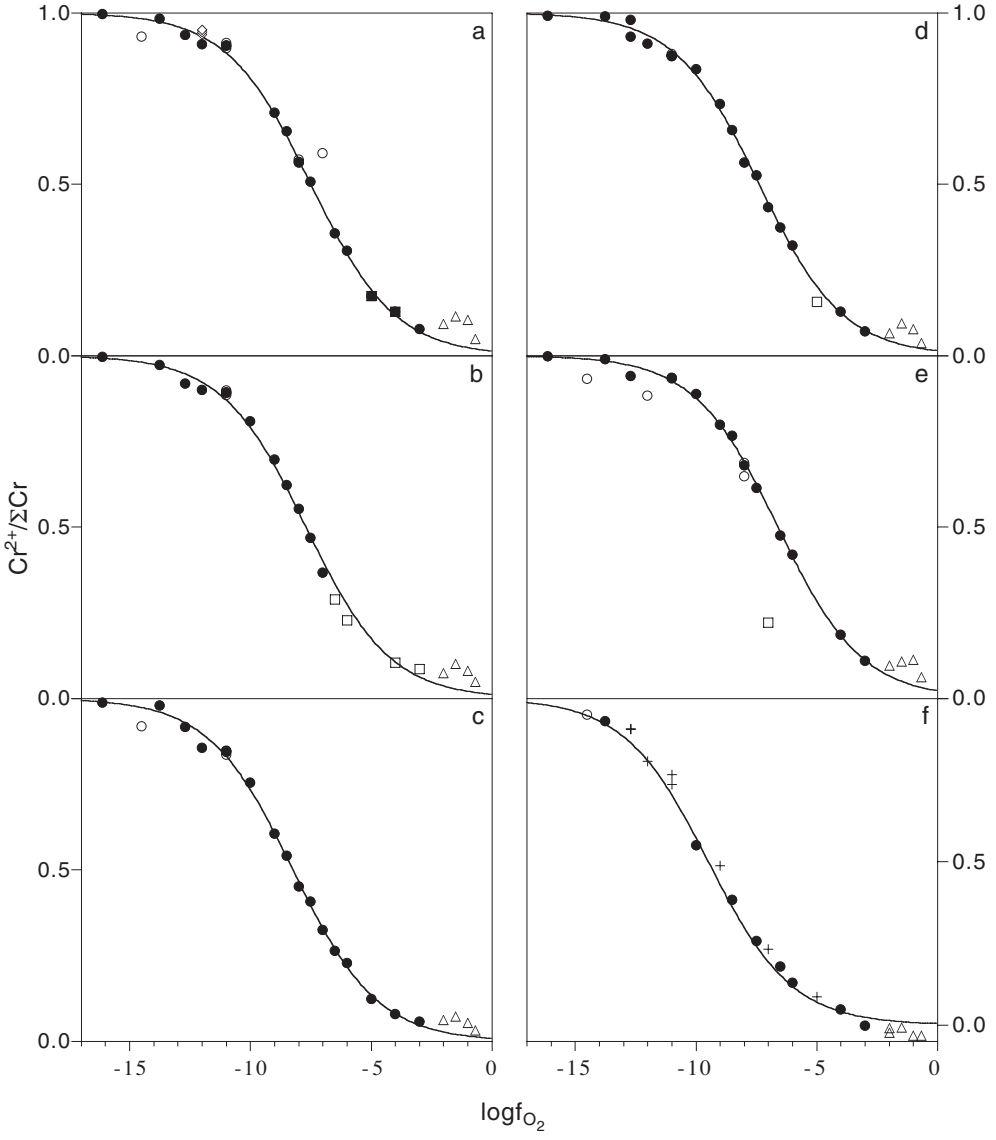

FIGURE 5. $Cr^{2+}/\Sigma Cr$ as a function of $\log f_{O_2}$ for (**a**) AD, (**b**) AD + Fo, (**c**) AD + Wo, (**d**) AD + En, (**e**) AD + Qz, and (**f**) AD + Rt. The solid lines are the best fits to the data using Equation 7 with the derivative area ($A_{1s/4s}$) being converted to $Cr^{2+}/\Sigma Cr$ using Equation 6 and the constants in Table 4. Points included in the fits are indicated by solid symbols. Samples containing Cr-spinel (open squares) and Cr^{6+} (Δ) are indicated. The fit in (**f**) is to AD + Rt (20%) with points for AD + Rt (10%) being given by +. The average of the replicate points shown for $\log f_{O_2} = -11$ was used in each fit. At $\log f_{O_2} = -12$ in (**a**) four additional points representing different Cr concentrations are given by open diamonds, and at $\log f_{O_2} = -8$ in (**a**) and (**e**) three points are shown corresponding to different equilibration times.

for the addition of Cr^{3+} in crystals to a constant melt Cr^{2+}/Cr^{3+} ratio determined by the $\log f_{O_2}$. The sigmoidal curves shown in Figures 5a–f are collated in Figure 6 to emphasize the differences in $\log K'$ for the compositions.

Spectra were also recorded for the AD composition, equilibrated at $\log f_{O_2} = -12$, containing 0.1, 0.2, 0.5, or 1.0 wt% ΣCr. The $A_{1s/4s}$ values and resulting $Cr^{2+}/\Sigma Cr$ ratios are identical, as shown in Figure 5a. This indicates Henry's Law behavior over this concentration range when Cr^{2+} is the dominant species. It is not possible to verify experimentally Henry's Law behavior for Cr^{3+} under oxidized conditions since increasing ΣCr promotes the crystallization of spinel. However, the experimentally determined exponent of 1/4 indicates the expected Henry's Law behavior over the entire $\log f_{O_2}$ range since any deviation from the theoretical behavior (i.e., constant $\gamma_{Cr^{3+}O_{1.5}}$ and $\gamma_{Cr^{2+}O}$) would change $n/4$. This has been observed for Fe^{2+}/Fe^{3+} in silicate melts at high ΣFe (Kilinc et al. 1983; Jayasuriya et al. in review). The ideal behavior of Cr in this study indicates that fluctuations in ΣCr between samples (e.g., due to volatility at high f_{O_2}s) will not affect the results. Several additional glasses were prepared as a function of equilibration time at $\log f_{O_2} = -8$. The $Cr^{2+}/\Sigma Cr$ ratios of AD samples equilibrated for 16 and 75 h are identical to that of the sample used in the $\log f_{O_2}$ series (Fig. 5a). For AD + Qz (the most viscous melt), the $Cr^{2+}/\Sigma Cr$ ratio after 13 hours is only slightly less than the value after 72 h (Fig. 5e). These results indicate that samples fully equilibrate with the imposed $\log f_{O_2}$ in less than 24 h.

Discussion

Cr is the only redox variable element in these glasses (apart from Ti in AD + Rt) and the systematic variation in glass color with $\log f_{O_2}$ indicates changes in the Cr oxidation state. The colors are consistent with those reported previously for Cr^{2+} and Cr^{3+} in silicate glasses (Schreiber and Haskin 1976). The trend in color suggests that optical absorption spectroscopy could be used to quantify $Cr^{2+}/\Sigma Cr$, however, in general this method only allows the qualitative identification of oxidation state ratios with errors ranging from 10–25% (Schreiber et al. 1987). In the case of Cr, the extraction of quantitative ratios is further complicated by overlapping spectral bands (Schreiber and Haskin 1976). Attempts at quantifying $Cr^{2+}/\Sigma Cr$ by optical spectroscopy in the present study were unsuccessful.

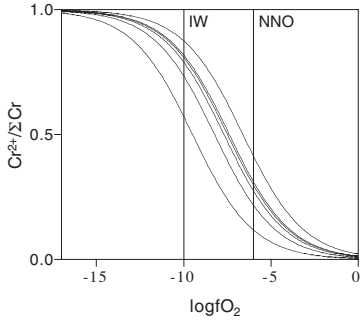

Figure 6. Compilation of the best fit curves shown in Figure 5 for, in order of increasing $\log f_{O_2}$, AD + Rt (20%), AD + Wo, AD + Fo, AD, AD + En, and AD + Qz. The vertical lines indicate values of the iron-wüstite (IW) and nickel-nickel oxide (NNO) log buffers at 1400 °C.

The quantification of $Cr^{2+}/\Sigma Cr$ in this work is based on the identification of a spectral feature that is found to correlate with the expected variation of $Cr^{2+}/\Sigma Cr$ with $\log f_{O_2}$. Modeling of the electronic transitions comprising the XANES edge has not been attempted. The ab-initio calculation of the edge, or attempts to fit the edge to various possible transitions, is complicated by the range of coordination geometries that may occur in a glass. They are also far more involved than the simple empirical approach described. Since we are not trying to model the edge structure the method used for normalizing the spectra is unimportant. A consequence, however, of crest normalization is that fitting an intermediate spectrum to a linear combination of the end-member spectra does not yield the correct $Cr^{2+}/\Sigma Cr$ values. This results, presumably, from differences in the intensity of the transitions which comprise the crest for each oxidation state, causing a scaling of the contribution of each component in the fit.

The simplicity of the fitting procedure benefits greatly from the linear correlation between $A_{1s/4s}$ and $Cr^{2+}/\Sigma Cr$, which simply scales the raw data to values of $Cr^{2+}/\Sigma Cr$ between 0 and 1 in Figure 5. This is not necessarily expected given the potential contribution of the $1s \rightarrow 3d$ transition and absorption edge background to the area of the derivative peak. The fact that the correlation is linear suggests that the feature is almost entirely due to the presence of Cr^{2+}. The appearance of Cr^{6+} does, however, contribute to the derivative spectrum since the $1s \rightarrow 3d$ transition overlaps the derivative range (Fig. 4, Cr^{6+}). This results in deviations from the calculated $Cr^{2+}/\Sigma Cr$ values for those samples containing Cr^{6+} (Fig. 5). However, the net effect is small since the derivative area of a symmetrical peak is ~0. The presence of minor Cr^{6+} in the nominal $Cr^{2+}/\Sigma Cr = 0$ end-member of the physical mixture calibration curve (Fig. 3) is expected to be negligible. The errors associated with sample preparation, the measurement technique, and $Cr^{2+}/\Sigma Cr$ values ($\log K'$), are all small and the scatter of the individual data points in Figure 5 from the theoretical best fit indicates that $\sigma(Cr^{2+}/\Sigma Cr) \sim 0.015$. This precision is comparable to that achieved for $Fe^{2+}/\Sigma Fe$ in silicate glasses by redox titrations (Kilinc et al. 1983) and Mössbauer spectroscopy under optimal conditions (Berry et al. 2003a; Jayasurya et al. in review). The agreement between the results of the best fit to the data and the theoretical slope ($n/4$) of 1/4 suggests that the method is accurate as well as precise.

In Equation 5 the parameter $n/4$ controls the slope of the sigmoidal curve and thus defines the $\log f_{O_2}$ range over which the oxidation (or reduction) occurs, while the position of the curve relative to the $\log f_{O_2}$ axis is determined by $\log K'$. The electrochemical reduction potential of a metal in a melt, which can be thought of in an analogous way to redox potentials in aqueous solutions (both oxide solvents), is defined as $-\log K'$ (Schreiber 1987). The value of $-\log K'$ varies with the redox couple (element and oxidation state) as well as the melt composition (Fig. 6), however, the relative order of redox couples in the electrochemical series is approximately fixed and similar to that in solutions (Schreiber 1987). The reduction potential, or $-\log K'$, of Cr^{3+}/Cr^{2+} in a melt composition similar to AD + Qz at 1500 °C was determined to be –1.6 (Schreiber 1987), consistent with our value of –1.656. For comparison, the reduction potential of Fe^{3+}/Fe^{2+} in this composition is –0.4 .

If $A_{1s/4s}$ is entirely due to Cr^{2+} then a_0 should be 0, with a_1

corresponding to the inverse of the maximum value of $A_{1s/4s}$, at $Cr^{2+}/\Sigma Cr = 1$. The intercept constant a_0 is ~0 (Table 4) with the non-zero value reflecting the contribution of the edge background to the derivative. a_0 is approximately constant for all compositions except those containing TiO_2 which exhibit a slight difference in edge profile. Figure 6 indicates that melt composition influences the reduction potential of Cr^{2+} at a given $\log f_{O_2}$. A component of this compositional effect is the differing capabilities of the melt to allow the distorted coordination sites necessary to stabilize the Cr^{2+} electronic configuration (Jahn-Teller effect). The intensity of the $1s \rightarrow 4s$ transition ($A_{1s/4s}$ or ~ $1/a_1$) for the fully reduced samples ($Cr^{2+}/\Sigma Cr = 1$) is related to the magnitude of the distortion from octahedral coordination since the transition is symmetry forbidden. The largest values of $A_{1s/4s}$ are for AD + Qz and AD + En and the smallest for AD + Wo and AD + Rt. This is in general agreement with the stability order ($\log K'$) in Figure 6; the largest derivative areas are associated with the greatest distortion of Cr^{2+} from octahedral symmetry, indicating increased electronic stabilization, and stability to higher values of $\log f_{O_2}$. The degree of distortion or stabilization will influence $\gamma_{Cr^{2+}O}$ and hence $\log K'$ (from Equation 4), although variations in $\log K'$ may result from the effects of melt composition on both $\gamma_{Cr^{2+}O}$ and $\gamma_{Cr^{3+}O_{1.5}}$.

The stabilization of Cr^{2+} ($\log K'$) correlates with SiO_2 and in particular $SiO_2 + Al_2O_3$ or the mole fraction (Si + Al)/O. It has been shown previously that reduced valence states are stabilized by large values of (Si + Al)/O (Lauer and Morris 1977), consistent with the results of the present study. There is no clear trend with the polymerization parameter NBO/T (non-bridging O atoms/tetrahedrally coordinated cations). The effect of TiO_2 on the stability of Cr^{2+} is significant, but complicated by the possibility of the charge transfer (electron exchange) reaction $Ti^{3+} + Cr^{3+} = Ti^{4+} + Cr^{2+}$, which should proceed from left to right according to melt reduction potentials (Schreiber 1987). The occurrence of this electron exchange is supported by the distinctive brown/black color of the Ti-bearing samples prepared under reducing conditions where Ti^{3+} may be expected. Ti^{3+} imparts a pale purple color to glasses of this type, in contrast to the intense color observed in our samples, which is consistent with a strongly allowed charge transfer reaction and interaction with Cr. However, this reaction should produce excess Cr^{2+} from Ti^{3+} on cooling, resulting in higher $Cr^{2+}/\Sigma Cr$ values than in the Ti-free compositions at a given $\log f_{O_2}$, which is opposite to what is observed. The expected stabilization of Cr^{2+} in Ti-bearing compositions may be counteracted by the effect of the change in melt composition on $\log K'$. Cr^{2+} stability in quenched glasses may therefore be controlled by a combination of the melt composition, the related melt structure (coordination site), and interactions with other redox variable species (Schreiber et al. 1987). At this stage the relative importance of these factors are unclear and a more detailed study on the effect of melt composition is planned.

Cr^{6+} first appears in the $\log f_{O_2} = -2$ sample (Table 3) for all compositions. The $\log K'$ of the Cr^{6+}/Cr^{3+} reaction is expected to depend upon composition, thus changing the $\log f_{O_2}$ where Cr^{6+} first occurs for each sample. This is not observed, but may reflect the resolution of the experiments since the oxidation is a $3e^-$ process ($n = 3$ in Equation 1) and the transition from Cr^{3+} to Cr^{6+} will occur over a much narrower $\log f_{O_2}$ range than that of Cr^{2+} to Cr^{3+}. A compositional dependence on $Cr^{6+}/\Sigma Cr$ is indicated, however, by variations in the height of the $1s \rightarrow 3d$ feature between samples at constant f_{O_2} (e.g., at $\log f_{O_2} = -0.68$). For a constant Cr^{6+} site (as expected for CrO_4^{2-}) the $1s \rightarrow 3d$ transition intensity should be directly proportional to $Cr^{6+}/\Sigma Cr$. The order in which the compositions stabilize Cr^{6+} is approximately equivalent to that for Cr^{3+} (except for AD + Rt), indicating intrinsic differences in the capacity of each melt to stabilize oxidized or reduced states.

The good agreement of most points with the fit, especially in the region where $Cr^{2+}/\Sigma Cr$ is changing quickly (~ $\log f_{O_2} = -8$), suggests that for work on additional compositions it should be possible to define the sigmoidal curve (and hence determine $\log K'$) from a limited number of samples. A reduced and oxidized sample would allow a_0 and a_1 to be determined while the position of the curve on the $\log f_{O_2}$ axis ($\log K'$) could be constrained by points at $\log f_{O_2} = -7$ and -9. $Cr^{2+}/\Sigma Cr$ for a sample prepared at $\log f_{O_2} = -16.13$ can be confidently assigned to 1 while the $\log f_{O_2}$ of the oxidized end-member could be selected based on composition to minimize the probability of forming either Cr^{6+} or spinel. Further, if a_0 is assumed to be 0.029 (Table 4) then an oxidized point is unnecessary. This simple procedure could be used to determine $\log K'$ efficiently for an expanded range of melt compositions to investigate the chemical and structural parameters that stabilize Cr^{2+}. To a first approximation, it should also be possible to determine a relative stability order from the derivative areas at a value of $\log f_{O_2}$, such as –8, where $Cr^{2+}/\Sigma Cr$ is changing rapidly.

The results of this work are consistent with those of Schreiber and Haskin (1976) but significantly more accurate over the entire range of $Cr^{2+}/\Sigma Cr$ values [$\sigma(Cr^{2+}/\Sigma Cr) = 0.015$ compared to 0.05–0.10]. At 1400 °C the $\log f_{O_2}$ values of the nickel-nickel oxide (NNO) (or quartz-fayalite-magnetite; QFM) and iron-wüstite (IW) buffers, which define the range of typical terrestrial magmas, are approximately –6 and –10 respectively. As can be seen from Figure 6, significant Cr^{2+} is observed under these conditions for all compositions. This is consistent with the change in Cr content of Fe-bearing liquids in equilibrium with spinel over this f_{O_2} range (Barnes 1986; Roeder and Reynolds 1991; Hanson and Jones 1998; Poustovetov and Roeder 2000). In these partitioning experiments Cr^{3+}/Cr^{2+} was determined from fits to Equations similar to 3. The resulting exponent in Fe-bearing systems is approximately 0.25, although the presence of Fe^{3+} appears to suppresses the occurrence of Cr^{2+} to lower $\log f_{O_2}$ values (i.e., a shift of the sigmoidal curve, or change in $\log K'$) (Hanson and Jones 1998). This interpretation assumes that $Cr^{2+}/\Sigma Cr = 0$ at NNO, however, other work has estimated $Cr^{2+}/\Sigma Cr = 0.3$ at QFM (Roeder and Reynolds 1991). The experimentally determined $n/4$ varies from ~0.22–0.28 and $\log K'$ from ~2.0–2.9 (Roeder and Reynolds 1991; Hanson and Jones 1998). In other models the comparability of $n/4$ and $\log K'$ are less clear due to the incorporation of temperature and compositional parameters (Barnes 1986; Poustovetov and Roeder 2000). The effect of Fe^{3+} and the subsequent amount of Cr^{2+} present in natural magmas remains uncertain. The $\log K'$s determined for the Fe-bearing systems are broadly consistent with those reported here for Fe-free compositions, noting differences in temperature, the treatment of $n/4$ as both fixed at 0.25 and as a variable, and the possibility of a

change in slope due to the interaction with Fe^{3+}. At higher $\log f_{O_2}$ values where Fe^{3+} becomes increasingly important, a reduction in the amount of Cr^{2+} would result in a steepening of the sigmoidal curve and an increase in $n/4$. The inferred presence of Cr^{2+} in Fe-bearing melts despite its absence in the quenched glasses, suggests that the electron exchange reaction $Cr^{2+} + Fe^{3+} \rightarrow Cr^{3+} + Fe^{2+}$ is temperature dependent. At high temperature Cr^{2+} and Fe^{3+} can co-exist, but on cooling the reaction proceeds completely to the right. This temperature effect was not anticipated by Schreiber and Haskin (1976) who assumed that the difference between the redox potentials of $Cr^{3+/2+}$ and $Fe^{3+/2+}$ at ambient temperature (which can explain the complete oxidation of Cr^{2+} by an excess of Fe^{3+}) would be maintained at the temperature of the melt. This is not the case and emphasizes the need for in situ experiments on Fe-bearing compositions.

In this work changes in the Cr *K*-edge XANES spectra for series of glasses prepared as a function of f_{O_2} were correlated with changes in the Cr oxidation state, allowing $Cr^{2+}/\Sigma Cr$ to be determined to better than ±0.015. Future work will be aimed at directly determining $Cr^{2+}/\Sigma Cr$ as a function of f_{O_2} in Fe-bearing melts (Berry et al. 2003b). This will allow the temperature dependence of the Cr/Fe electron exchange reaction and effect of Fe on $\log K'$ to be investigated. In general terms, this empirical approach based on identifying how XANES features vary with f_{O_2}, and hence oxidation state, has potential application to almost any element.

ACKNOWLEDGMENTS

Part of this work was performed at the Australian National Beamline Facility with support from the Australian Synchrotron Research Program, which is funded by the Commonwealth of Australia under the Major National Research Facilities Program. We thank G.J. Foran for valuable assistance with the XANES experiments, D.R. Scott for sample preparation, and N.G. Ware for electron microprobe analyses. A.J.B. also thanks the Australian Research Council for the award of a Fellowship.

REFERENCES CITED

Arcon, I., Mirtic, B., and Kodre, A. (1998) Determination of valence states of chromium in calcium chromates by using X-ray absorption near-edge structure (XANES) spectroscopy. Journal of the American Ceramic Society, 81, 222–224.

Bajt, S., Clark, S.B., Sutton, S.R., Rivers, M.L., and Smith, J.V. (1993) Synchrotron X-ray microprobe determination of chromate content using X-ray absorption near-edge structure. Analytical Chemistry, 65, 1800–1804.

Bajt, S., Sutton, S.R., and Delaney, J.S. (1994) X-ray microprobe analysis of iron oxidation states in silicates and oxides using X-ray absorption near edge structure (XANES). Geochimica et Cosmochimica Acta, 58, 5209–5214.

Barnes, S.J. (1986) The distribution of chromium among orthopyroxene, spinel and silicate liquid at atmospheric pressure. Geochimica et Cosmochimica Acta, 50, 1889–1909.

Berry, A.J., O'Neill, H.St.C., Jayasuriya, K.D., Campbell, S.J., and Foran, G.J. (2003a) XANES calibrations for the oxidation state of iron in a silicate glass. American Mineralogist, 88, 967–977.

Berry, A.J., Shelley, J.M.G., Foran, G.J., O'Neill, H.St.C., and Scott, D.R. (2003b) A furnace design for XANES spectroscopy of silicate melts under controlled oxygen fugacities and temperatures to 1773K. Journal of Synchrotron Radiation, 10, 332–336.

Brigatti, M.F., Galli, E., Medici, L., Poppi, L., Cibin, G., Marcelli, A., and Mottana, A. (2001) Chromium-containing muscovite: crystal chemistry and XANES spectroscopy. European Journal of Mineralogy, 13, 377–389.

Burns, V.M. and Burns, R.G. (1975) Mineralogy of chromium. Geochimica et Cosmochimica Acta, 39, 903–910.

Farges, F., Brown Jr., G.E., and Rehr, J.J. (1996) Coordination chemistry of Ti (IV) in silicate glasses and melts: I. XAFS study of titanium coordination in oxide model compounds. Geochimica et Cosmochimica Acta, 60, 3023–3038.

Foran, G.J., Garrett, R.F., Gentle, I.R., Creagh, D.C., Peng, J.B., and Barnes, G. T. (1998) Focusing monochromator and imaging plate camera for grazing incidence diffraction studies of thin films. Journal of Synchrotron Radiation, 5, 500–502.

Haggerty, S.E., Boyd, F.R., Bell, P.M., Finger, L.W., and Bryan, W.B. (1970) Opaque minerals and olivine in lavas and breccias from Mare Tranquillitatis. Proceedings of the Apollo 11 Lunar Science Conference, 1, 513–538.

Hanson, B. and Jones, J.H. (1998) The systematics of Cr^{3+} and Cr^{2+} partitioning between olivine and liquid in the presence of spinel. American Mineralogist, 83, 669–684.

Holzheid, A., Palme, H., and Chakraborty, S. (1997) The activities of NiO, CoO and FeO in silicate melts. Chemical Geology, 139, 21–38.

Kilinc, A., Carmichael, I.S.E., Rivers, M.L., and Sack, R.O. (1983) The ferric-ferrous ratio of natural silicate liquids equilibrated in air. Contributions to Mineralogy and Petrology, 83, 136–140.

Krause, M.O. and Oliver, J.H. (1979) Natural widths of atomic K and L levels, Kα X-ray lines and several KLL Auger lines. Journal of Physical and Chemical Reference Data, 8, 329–338.

Lauer, H.V. and Morris, R.V. (1977) Redox equilibria of multivalent ions in silicate glasses. Journal of the American Ceramic Society, 60, 443–451.

Levina, A., Foran, G.J., and Lay, P.A. (1999) X-ray absorption spectroscopic studies of the Cr(IV) 2-ethyl-2-hydroxybutanoato(1-) complex. Chemical Communications, 2339–2340.

Li, J.-P., O'Neill, H.St.C., and Seifert, F. (1995) Subsolidus phase relations in the system MgO-SiO_2-Cr-O in equilibrium with metallic Cr, and their significance for the petrochemistry of chromium. Journal of Petrology, 36, 107–132.

Liang, Y. and Elthon, D. (1990) Evidence from chromium abundances in mantle rocks for extraction of pricrite and komatiite melts. Nature, 343, 551–553.

O'Neill, H.S.C. and Eggins, S.M. (2002) The effect of melt composition on trace element partitioning: an experimental investigation of the activity coefficients of FeO, NiO, CoO, MoO_2 and MoO_3 in silicate melts. Chemical Geology, 186, 151–181.

O'Neill, H.S.C. and Mavrogenes, J.A. (2002) The sulfide capacity and the sulfur content at sulfide saturation of silicate melts at 1400 °C and 1 bar. Journal of Petrology, 43, 1049–1087.

Peterson, M.L., Brown Jr., G.E., Parks, G.A., and Stein, C.L. (1997) Differential redox and sorption of Cr(III/VI) on natural silicate and oxide minerals: EXAFS and XANES results. Geochimica et Cosmochimica Acta, 61, 3399–3412.

Poustovetov, A.A. and Roeder, P.L. (2000) The distribution of Cr between basaltic melt and chromium spinel as an oxygen geobarometer. Canadian Mineralogist, 39, 309–317.

Roeder, P.L. and Reynolds, I. (1991) Crystallization of chromite and chromium solubility in basaltic melts. Journal of Petrology, 32, 909–934.

Schreiber, H.D. (1987) An electrochemical series of redox couples in silicate melts: a review and applications to geochemistry. Journal of Geophysical Research, 92, 9225–9232.

Schreiber, H.D. and Haskin, L.A. (1976) Chromium in basalts: Experimental determination of redox states and partitioning among synthetic silicate phases. Proceedings of the 7th Lunar Science Conference, p. 1221–1259.

Schreiber, H.D., Merkel Jr., R.C., Schreiber, V.L., and Balazs, G.B. (1987) Mutual interactions of redox couples via electron exchange in silicate melts: models for geochemical melt systems. Journal of Geophysical Research, 92, 9233–9245.

Shulman, R.G., Yafet, Y., Eisenberger, P., and Blumberg, W.E. (1976) Observation and interpretation of X-ray absorption edges of iron compounds and proteins. Proceedings of the National Academy of Science, 73, 1384–1388.

Sutton, S.R., Jones, K.W., Gordon, B., Rivers, M.L., Bajt, S., and Smith, J.V. (1993) Reduced chromium in olivine grains from lunar basalt 15555: X-ray absorption near edge structure (XANES). Geochimica et Cosmochimica Acta, 57, 461–468.

Szulczewski, M.D., Helmke, P.A., and Bleam, W.F. (1997) Comparison of XANES analyses and extractions to determine chromium speciation in contaminated soils. Environmental Science and Technology, 31, 2954–2959.

Waychunas, G.A., Apted, M.J., and Brown Jr., G.E. (1983) X-ray K-edge absorption spectra of Fe minerals and model compounds: near edge-structure. Physics and Chemistry of Minerals, 10, 1–9.

Wilke, M., Farges, F., Petit, P.-E., Brown Jr., G.E., and Martin, F. (2001) Oxidation state and coordination of Fe in minerals: an Fe K-XANES spectroscopic study. American Mineralogist, 86, 714–730.

Wong, J., Lytle, F.W., Messmer, R.P., and Maylotte, D.H. (1984) K-edge absorption spectra of selected vanadium compounds. Physical Review B, 30, 5596–5609.

MANUSCRIPT RECEIVED JULY 29, 2003
MANUSCRIPT ACCEPTED NOVEMBER 7, 2003
MANUSCRIPT HANDLED BY SIMONA QUARTIERI